# MRI mapping of hemodynamics in the human spinal cord

Kimberly J. Hemmerling[12], Mark A. Hoggarth[13], Milap S. Sandhu[45], Todd B. Parrish[26], Molly G. Bright[12]

**Author Affiliations:**

[1] Department of Physical Therapy and Human Movement Sciences, Feinberg School of Medicine, Northwestern University, Chicago, IL, United States

[2] Department of Biomedical Engineering, McCormick School of Engineering, Northwestern University, Evanston, IL, United States

[3] Department of Physical Therapy, North Central College, Naperville, IL, United States

[4] Shirley Ryan Ability Lab, Chicago, IL, United States

[5] Department of Physical Medicine and Rehabilitation, Feinberg School of Medicine, Northwestern University, Chicago, IL, United States

[6] Department of Radiology, Feinberg School of Medicine, Northwestern University, Chicago, IL, United States

**Abstract**

Impaired spinal cord vascular function contributes to numerous neurological pathologies, making it important to be able to noninvasively characterize these changes. Here, we propose a functional magnetic resonance imaging (fMRI)-based method to map spinal cord vascular reactivity (SCVR). We used a hypercapnic breath-holding task, monitored with end-tidal $CO_2$ ($P_{ET}CO_2$), to evoke a systemic vasodilatory response during concurrent blood oxygenation level-dependent (BOLD) fMRI. SCVR amplitude and hemodynamic delay were mapped at the group level in 27 healthy participants as proof-of-concept of the approach, and then in two highly-sampled participants to probe feasibility/stability of individual SCVR mapping. Across the group and the highly-sampled individuals, a strong ventral SCVR amplitude was initially observed without accounting for local regional variation in the timing of the vasodilatory response. Shifted breathing traces ($P_{ET}CO_2$) were used to account for temporal differences in the vasodilatory response across the spinal cord, producing maps of SCVR delay. These delay maps reveal an earlier ventral and later dorsal response and demonstrate distinct gray matter regions concordant with territories of arterial supply. The SCVR fMRI methods described here enable robust mapping of spatiotemporal hemodynamic properties of the human spinal cord. This noninvasive approach has exciting potential to provide early insight into pathology-driven vascular changes in the cord, which may precede and predict future irreversible tissue damage and guide the treatment of several neurological pathologies involving the spine.

**Keywords:** spinal cord, vascular reactivity, fMRI, hypercapnia, hemodynamics

**Funding:** Research supported by the Craig H. Neilsen Foundation (595499). KJH was supported by an NIH NIBIB-funded training program (T32EB025766) and NINDS-funded predoctoral fellowship (F31NS134222).

**Acknowledgements:** This work was supported by the Center for Translational Imaging at Northwestern University. The authors would like to thank Robert L. Barry for contributions to the development of our data preprocessing pipeline and Sameer Faruquee for contributions to data preprocessing.

**Corresponding Author:**
Kimberly J. Hemmerling
645 N. Michigan Ave., Suite 1100
Chicago, IL 60611
USA
khemmerling@northwestern.edu

## 1. Introduction

Impaired vascular function is a major contributor to multiple neurological pathologies involving the spinal cord, including traumatic spinal cord injury (1) and degenerative cervical myelopathy (2). It is therefore of great importance, for both basic research and clinical translation, to characterize these changes in blood supply to the spinal cord tissue. However, existing methods to noninvasively characterize vascular function in the human brain have not yet been successfully translated to the cord. In general, physiological and functional magnetic resonance imaging (fMRI) of the spinal cord has lagged the development of such methods in the brain. This has largely been due to the challenges typically associated with these methods, including the small size of the spinal cord, nearby sources of physiological noise, magnetic field inhomogeneities, and low signal to noise ratio (SNR) (3). More recently, technological and methodological developments have enabled more robust fMRI studies of the spinal cord, including mapping of sensory, motor, and resting-state neural activation patterns (4).

Despite these advances, MRI techniques for characterizing vascular properties of the spinal cord have remained somewhat limited. Dynamic susceptibility contrast (DSC) MRI, following injection of a gadolinium-based contrast agent, presents the gold standard for quantifying tissue perfusion and blood volume in the brain. Existing studies of vascular changes in the spinal cord of people with degenerative cervical myelopathy use this technique, showing sensitivity to the ischemic effects of cord compression (5, 6). However, due to the low SNR of DSC data in the cord, these works report a single non-quantitative value for the entire cord region, rather than quantifying and mapping absolute vascular metrics. Repeated scans may boost data quality, but they are not readily feasible in DSC due to the long wash-out time of the contrast agent and the growing safety concerns over repeated exposure to gadolinium-based contrast agents (7). Dynamic contrast enhanced (DCE) MRI measures the contrast agent accumulation (8); although more commonly used to look at tumors in the spine, preliminary work demonstrates the potential of DCE to evaluate spinal cord perfusion after compression, but the technique is still in early development (9).

A contrast-free alternative, arterial spin labeling (ASL) MRI, shows excellent promise in the spinal cord injured rat (10, 11), and in the human spinal cord in early conference proceedings (12, 13). However, despite rapid growth of ASL for perfusion mapping of the brain, the unique challenges of spinal cord ASL have continued to hinder progress (e.g., low SNR, variable vascular anatomy for labelling and delay modeling, B0 inhomogeneity influencing labeling efficiency) (10). Recent exciting advances in pre-clinical studies are renewing interest and enthusiasm for spinal cord ASL in humans, but substantial methodological development is still needed before this technique can reliably shed light on human spinal cord pathophysiology (10). Another current research area is high-field intra-voxel incoherent motion (IVIM) MRI, which has shown promising maps of healthy human spinal cord perfusion, albeit in a single slice and at the less common ultra-high field strength (7T) (14).

Here, we propose an alternative technique to map vascular function throughout the human spinal cord using blood oxygenation level-dependent (BOLD) fMRI, a well-established neuroimaging technique that is sensitive to changes in regional blood flow, and which has been successfully adapted and optimized for spinal cord neural activation mapping in recent years (4). Specifically, we use fMRI to map spinal cord vascular reactivity (SCVR), the cord's blood flow responsiveness to a systemic vasodilatory stimulus. In the brain, vascular reactivity and hemodynamic delay measured with BOLD fMRI have been established as robust metrics of cerebrovascular function (15, 16). However, techniques for adapting these methods to the spinal cord are not yet well established. Two prior spinal cord fMRI studies have used gas inhalation challenges to modulate the vascular system, however, these are smaller studies (<10 participants) without all modern acquisition and modeling innovations, and do not map the distribution of vascular reactivity and delay (17, 18).

In this study, we use advanced spinal cord fMRI methods to measure the local vasodilatory response to hypercapnia and map SCVR across the cervical spinal cord in healthy adults. We evoke systemic hypercapnia (elevated $CO_2$) with simple breath-holding tasks (15), precluding the need for gas delivery systems. By recording end-tidal $CO_2$ ($P_{ET}CO_2$) levels during scanning, we form a subject- and scan-specific model of the hypercapnia achieved by our breath-holding protocol. By determining the optimal shift between this model and each fMRI voxel's timeseries, we produce more accurate estimates of SCVR amplitude and an additional complementary metric of hemodynamic delay (19).

In this pioneering work, we explore SCVR from two approaches. In the first **(Group SCVR)**, we aim to establish proof-of-concept of our SCVR approach in the cervical spinal cord, mapping the group-level BOLD response from a cohort of 27 healthy participants. Participants completed 2 breath-holding task fMRI runs across 2 sessions. However, to provide more clinically relevant information, SCVR needs to be characterized in individuals. Therefore, in the second study **(Individual SCVR)** we focus on 2 highly-sampled participants to evaluate feasibility of individual SCVR mapping. Each participant completed 18 breath-holding task fMRI runs across 3 MRI sessions.

In both of these approaches, we mapped SCVR and the associated hemodynamic delay using a lagged general linear model (GLM) strategy. To map SCVR amplitude, $P_{ET}CO_2$ task regressors were fit to the fMRI timeseries in a GLM (also incorporating state-of-the-art denoising via nuisance regression). Output parameter estimates (%BOLD per change in $P_{ET}CO_2$ in mmHg) were combined across the group (Group SCVR) or across individuals' runs (Individual SCVR). Hemodynamic delay mapping was achieved by temporally shifting the $P_{ET}CO_2$ regressor and fitting each shifted regressor to the fMRI timeseries. Then, the shift with the best fit across participants (Group SCVR) or runs (Individual SCVR) was used to create a hemodynamic delay map, representing regional variation in the timing of this vascular response across the spinal cord. The SCVR amplitude estimate at this optimal shift was considered the "delay-corrected" SCVR.

We present maps of SCVR amplitude and hemodynamic delay at the group-level and in highly-sampled individuals, in the C5–C8 segments of the human cervical spinal cord. Furthermore, by thresholding the hemodynamic delay maps, we produce noninvasive maps of vascular territories in the human spinal cord, showing agreement with territory maps extrapolated from invasive and preclinical studies. Our scanning methods are readily implemented on most 3T MRI scanners, making this approach to characterizing spinal cord hemodynamics immediately available for basic science and translational research into human spinal cord neurovascular physiology and pathology.

## 2. Results

**Group SCVR amplitude.** The $P_{ET}CO_2$ task regressor was generated by identifying end-tidal values in the $CO_2$ recording for each fMRI run and convolving with the canonical hemodynamic response function (HRF). First-level GLMs were calculated for each subject's scan using $P_{ET}CO_2$ task regressors and nuisance regressors (motion, RETROICOR, cerebrospinal fluid (CSF)). These task regressors allow SCVR mapping in standard semi-quantitative units of %BOLD/mmHg. Then, the output parameter estimate maps for $P_{ET}CO_2$ were averaged together within subject. Group-level SCVR was mapped in PAM50 template space by a non-parametric 1-sample t-test with threshold-free cluster enhancement (TFCE) **(Fig. 1)**. SCVR is distributed predominantly within the ventral spinal hemicord, primarily in or near the gray matter ventral horns, and spread throughout the longitudinal extent of the cervical spinal cord.

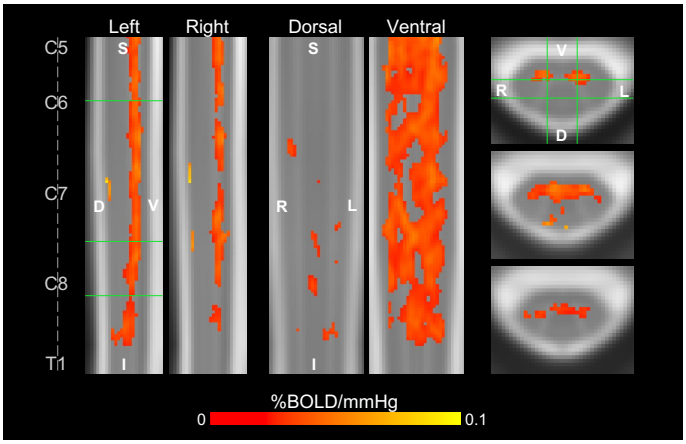


***Fig. 1. Group-level SCVR amplitude map.*** *Significant SCVR is shown in units of %BOLD/mmHg (p<0.05, FWE-corrected). Two sagittal, two coronal, and three axial slices are shown (green lines indicate location of slices). Approximate centers of spinal cord segments are indicated. (FWE=family-wise error, S=superior, I=inferior, D=dorsal, V=ventral, L=left, R=right).*

**Individual SCVR amplitude.** The $P_{ET}CO_2$ regressors show high task compliance across 18 fMRI task runs for the two highly-sampled subjects **(Fig. 2A,E)**. First-level GLMs were calculated identically to above, and then the 18 output parameter estimate maps were collated. Individual SCVR amplitude maps in PAM50 template space were also generated with a non-parametric 1-sample t-test with TFCE **(Fig. 2B,F)**. SCVR amplitude for both highly-sampled subjects has a similar spatial distribution to the group-level maps, with a high density of significantly responding voxels in the ventral gray matter tissue. However, the amplitude for Subject 1 is visibly higher than for Subject 2.

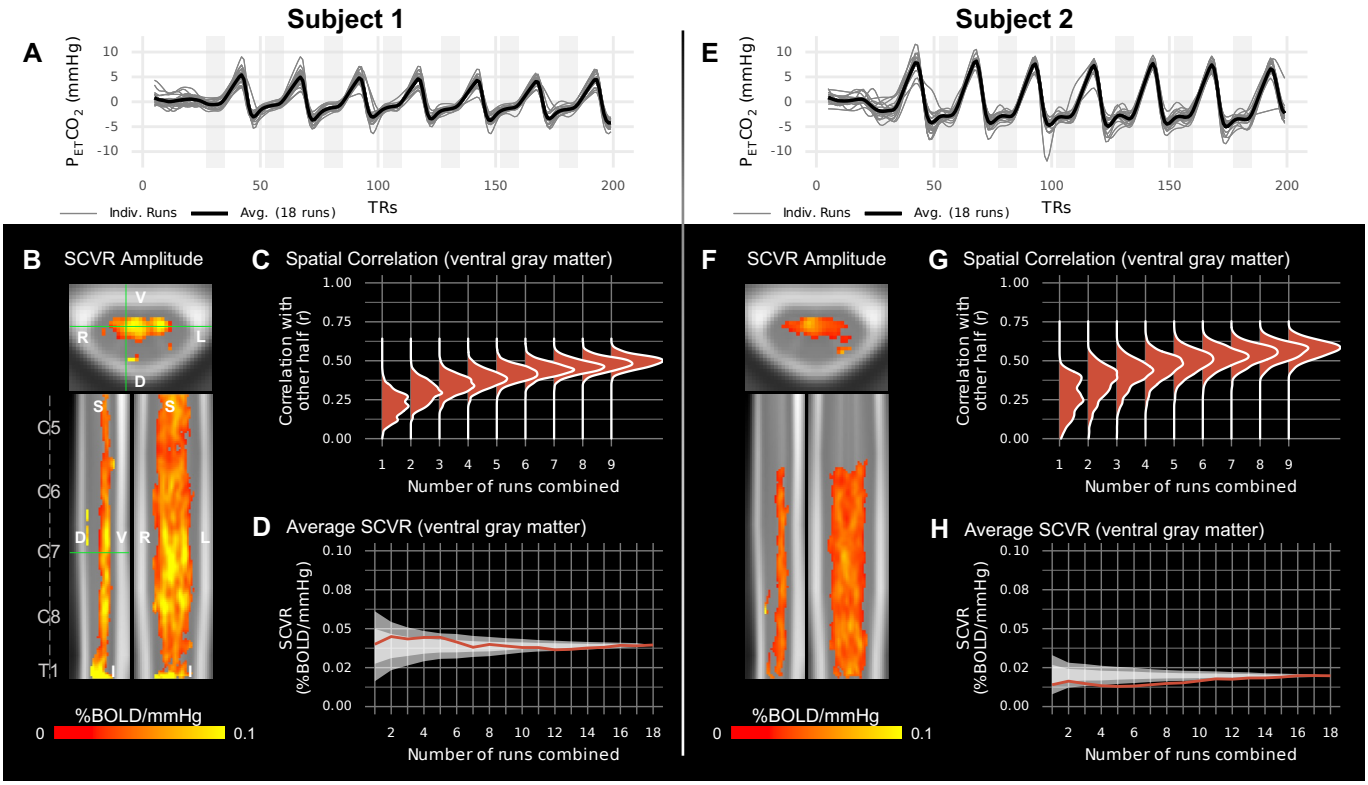


***Fig. 2. SCVR mapping in two highly-sampled subjects. (A,E)*** *$P_{ET}CO_2$ regressors (convolved with the canonical HRF and demeaned) for 18 breath-holding task runs and their average.* ***(B,F)*** *Maps of SCVR amplitude in axial, sagittal, and coronal planes (FWE-corrected, $p<0.05$). Spinal cord segments and slice locations (green lines) are indicated.* ***(C,G)*** *Split-halves spatial correlation of gray matter SCVR amplitude for varying number of runs combined (1-9) vs. other half combined (9 runs).* ***(D,H)*** *Average SCVR as runs are sequentially combined in the order they were acquired (red line) and in randomly shuffled orders (shaded areas; ±1SD and ±2SD).*

To investigate the reliability of SCVR amplitude estimates generated from subsets of the highly-sampled individual datasets, a split halves analysis was performed. Modeled after Laumann et al. 2015 (20), this was done by randomly and repeatedly splitting gray matter SCVR estimates for the 18 runs into two halves and comparing combinations of one half (1-9 runs) to the other half combined (9 runs). A spatial Pearson correlation within ventral gray matter voxels was used to compare the two halves **(Fig. 2C,G)**. In both subjects, comparing SCVR estimates derived from only 1 run versus from 9 runs combined yields weak spatial correlation (median $r<0.3$). When comparing SCVR estimates from 6 runs combined versus 9 runs combined, this yields a moderate spatial correlation (median $r\approx0.4$-$0.6$). Looking at average SCVR as runs are incrementally combined, the variability initially rapidly decreases, and then more gradually **(Fig. 2D,H)**.

**Group SCVR delay.** The distinct ventral distribution of significant SCVR responses raises the question of whether variation in the timing of the SCVR response may be obscuring this effect in more dorsal regions. To investigate and account for temporal delays, first-level models were recalculated with shifted versions of the $P_{ET}CO_2$ task regressor (±10s, in increments of 2s) **(Fig. 3A)**. Group-level SCVR was calculated for each shift using the same method as above. The optimal shifts were identified, and the corresponding delay map and delay-corrected SCVR amplitude map were generated **(Fig. 3B, Fig. S1)**. (Note, this approach assumes that the timing of the voxelwise SCVR response is the same across all subjects.)

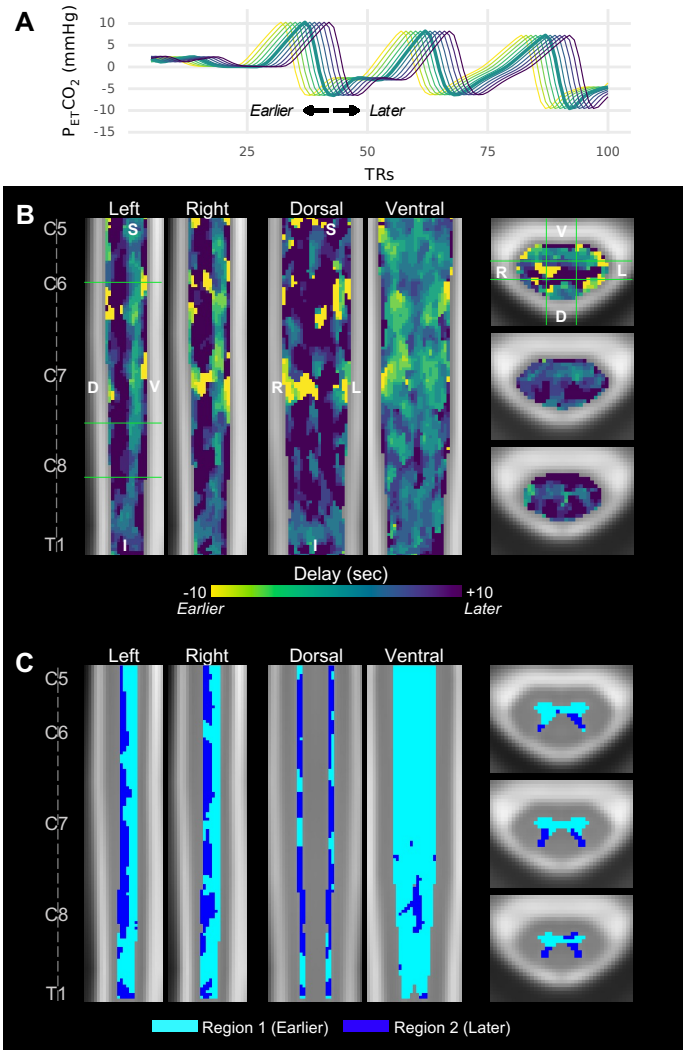


***Fig. 3. SCVR hemodynamic delay mapping at the group-level. (A)*** *Example of temporally shifted $P_{ET}CO_2$ regressors. The unshifted (no delay) $P_{ET}CO_2$ regressor (thick green line) and each tested shift ±10s, in 2s increments, are shown. Line colors correspond to the "Delay" colorbar in panel B. Full traces are truncated at 100 TRs for ease of visualization.* ***(B)*** *SCVR hemodynamic delay map (ranging ±10s, in increments of 2s). The same slices as Fig. 1 are shown.* ***(C)*** *Gray matter regional segmentation based on delay threshold.*

As anticipated, the delay-corrected SCVR amplitude map shows a more diffuse distribution of significantly responding voxels. Across all participants, the distribution of Group SCVR hemodynamic delay shows an earlier response in the ventral cord, and later in the dorsal cord. Moreover, these earlier and later responding regions appear to resemble the shape of the ventral and dorsal gray matter

horns, respectively. The average delay between the dorsal and ventral horns is approximately 5 seconds (2.5 times our sampling TR).

Using a histogram of gray matter SCVR delay, a delay threshold was manually defined; each voxel was labeled as Region 1 (sub-threshold, earlier response) or Region 2 (supra-threshold, later response), which comprises the delay-based gray matter segmentation **(Fig. 3C)**. The approximate boundary between the ventral and dorsal horns can be clearly observed.

**Individual SCVR delay.** Hemodynamic delay was mapped with the same methods as for Group SCVR. The SCVR delay maps for the two highly-sampled individuals show a similar ventral-dorsal spatial distribution as for Group SCVR **(Fig. 4A,E)**. The delay between dorsal and ventral gray matter is approximately 6 seconds and 7 seconds for Subject 1 and Subject 2, respectively. A delay-corrected SCVR amplitude map was created using the parameter estimates associated with the optimal shift for each voxel **(Fig. 4B,F)**, and shows a more diffuse spread of significantly responding voxels, as compared to Fig. 2B,F. The delay-corrected significant SCVR response from both highly-sampled individuals is also more extensive than the group SCVR delay-corrected map **(Fig. S1)**.

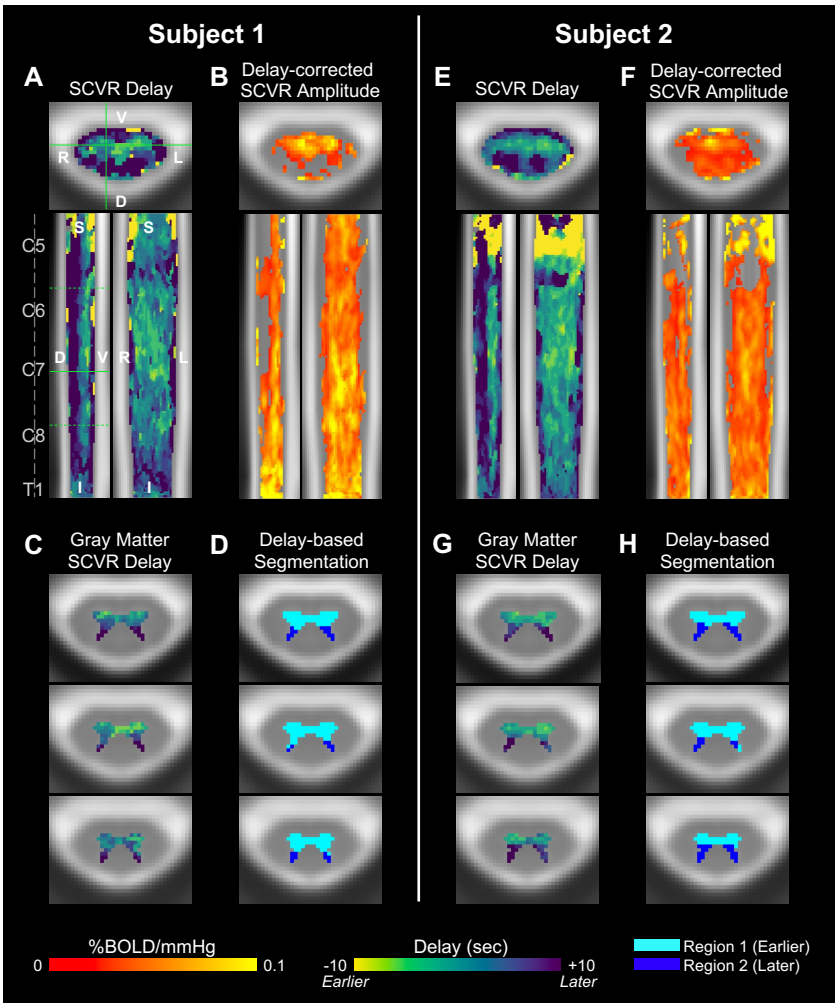


***Fig. 4. SCVR delay mapping in two highly-sampled subjects. (A,E)*** *SCVR delay map (ranging ±10s, in increments of 2s). Spinal cord segments and slice locations (solid green lines) are indicated. The three solid and dotted green lines in the sagittal view indicate axial slices in the lower panels.* ***(B,F)*** *Delay-corrected SCVR amplitude (FWE-corrected, p<0.05). The same slices as Fig. 2 are shown.* ***(C,G)*** *SCVR delay map within gray matter voxels.* ***(D,H)*** *Gray matter regional segmentation based on delay threshold.*

The individual subject SCVR hemodynamic delay maps, restricted to show gray matter voxels, clearly recapitulate the earlier and later responses in the ventral and dorsal horns, respectively **(Fig. 4C,G)**. Applying the thresholding approach described above, the ventral and dorsal boundary is defined, and agrees with the group-level results **(Fig. 4D,H)**.

## 3. Discussion

In this work, we used a breath-holding task to evoke systemic vasodilation and a corresponding BOLD fMRI response in the spinal cord, and then modeled SCVR amplitude and hemodynamic delay. Applying these methods in a cross-sectional cohort and in two highly-sampled individuals, we produced robust spatiotemporal maps of vascular function in the human cervical spinal cord. Our results reveal hemodynamic differences in ventral versus dorsal gray matter regions, consistent across individuals, suggesting that SCVR delay could delineate vascular territories in the cord.

**Spatial distribution of SCVR estimates.** SCVR modeled with $P_{ET}CO_2$ provides semi-quantitative information about the regional spinal cord hemodynamic response to a vasoactive stimulus. Cerebrovascular reactivity has already proven to deliver clinically relevant information about cerebrovascular health (15, 16), indicating the potential utility of similar measures for the spinal cord. In the healthy cohort examined in this study, the distribution of significant SCVR (without delay correction) is restricted to more ventral tissue, although extending throughout the longitudinal extent of our imaging field of view. Sensitivity of the SCVR technique in this region may be particularly relevant for early detection of vascular changes in patients with degenerative cervical myelopathy, as age-related cord compression and subsequent neurodegeneration is most prevalent in the ventral regions (21).

The significant ventral SCVR response is predominantly, but not strictly, localized to gray matter voxels. This agrees with observations of vascular reactivity in the brain, where the cerebrovascular reactivity amplitude is greater in gray matter versus white matter voxels due to it being more highly vascularized and having higher SNR (16). Early reports of BOLD signal changes in the spinal cord achieved with a hypercapnic gas inhalation challenge were roughly 0.17 %BOLD/mmHg (based on a reported 0.6 mean percent signal change with a 3.5mmHg mean $P_{ET}CO_2$ change (17)), as compared to 0.01 %BOLD/mmHg for the group SCVR across the whole spinal cord region-of-interest in this study. This difference may be due to smaller sample sizes inflating parameter estimates (22), or because of the different methods of averaging – our measure is obtained from the group level parameter estimates, so they are not directly comparable to the previous study. The mean ventral gray matter SCVR is about 0.02 %BOLD/mmHg, which is about an order of magnitude lower than similar mean gray matter cerebrovascular reactivity measures (23, 24) and is to be expected because of increased SNR in the brain.

The SCVR maps derived from the highly-sampled individuals reveal higher SCVR amplitude for Subject 1 compared to Subject 2. There is also a conspicuous absence of significant SCVR estimates in the superior spinal cord for Subject 2. The underlying reason for these differences in SCVR

amplitude is unclear and may represent differences in anatomy, physiology or regional fMRI signal quality.

**Reliability of SCVR measurements in individuals.** Individual SCVR amplitude maps were comprised of 18 fMRI runs, for which each participant completed a total of 126 individual breath-holds. Considering our long-term goal to use SCVR to provide clinical insight into neurological pathology development and progression, it is not reasonable to expect patients to undergo over 100 minutes of breath-hold fMRI. To assess the feasibility of clinical translation using our current SCVR acquisition strategy, we implemented a split halves analysis to probe the number of fMRI runs necessary to achieve reliable SCVR estimates. As shown in **Fig. 2**, the voxelwise spatial correlation in ventral gray matter begins to plateau at approximately 5-6 runs, indicating data from one scan session (34-41 min) may be sufficient to map SCVR. The high initial variability in average ventral gray matter SCVR is also substantially reduced at 5-6 runs combined. Although this duration may be limited to clinical research studies, we anticipate that future methodological improvements in acquisition, denoising, and machine learning will further decrease this scan time requirement and make SCVR mapping a viable clinical scan technique. Furthermore, there is relatively low variability in voxelwise SCVR within gray matter in these healthy individuals, and spatial correlations may be much higher in subjects with greater heterogeneity in SCVR values due to pathology.

**Hemodynamic delay maps resemble territories of vascular supply.** Because the hypercapnic breath-hold challenge evokes a systemic vasodilatory response, we expected a more widespread fMRI response throughout both ventral and dorsal spinal cord tissue. The absence of significant dorsal responses in **Figs. 1** and **2** allude to spatiotemporal variability in the relationship between our $P_{ET}CO_2$ model and the associated BOLD response across the spinal cord. Differences in timing could arise because of arterial transit time differences and local variability in the vasodilatory blood flow response and associated BOLD contrast changes. Maps of SCVR hemodynamic delay reveal local regional variation in the timing of the blood flow response that are consistent across our cohort, with earlier and later responses in the ventral and dorsal gray matter, respectively. Although BOLD fMRI is primarily sensitive to venous effects, the response to $CO_2$ is driven by arteriolar vasodilation. So, local timing differences may (at least in part) represent territories of arterial supply to the spinal cord.

Supplying approximately the ventral two-thirds of the cord is the <u>central system</u>, derived from the anterior spinal artery (ASA) (1). From the ASA, central sulcal arteries penetrate into the anterior median fissure (1, 25). Blood flows centrifugally, supplying the ventral gray matter, ventral aspect of the dorsal gray matter, and other white matter regions (1, 26). This aligns well with the spatial distribution of the earlier ventral gray matter response.

The approximate remaining one third of the cord is supplied by the peripheral system, derived from the paired posterior spinal arteries (PSAs) and pial arterial plexus (1). The ASA and PSAs contribute to an anastomosed network on the periphery of the spinal cord, the pial arterial plexus, from which vessels penetrate the spinal cord perpendicular to its surface (1, 26). Blood flows centripetally, supplying the dorsal aspect of the dorsal gray matter and other white matter regions (1, 26). This aligns well with the spatial distribution of the later SCVR responses. Additionally, by applying a simple threshold to the SCVR hemodynamic delay maps, we can cleanly delineate these two gray matter vascular territories: (1) areas with an earlier response of likely ASA supply (ventral horns and intermediate zone) and (2) areas with a later response of likely PSAs supply (dorsal horns).

**SCVR delay correction.** Not accounting for regional timing differences can bias vascular reactivity measurements (19). When accounting for SCVR hemodynamic delay by "correcting" the timing of the $P_{ET}CO_2$ regressor, we have a more optimal model of vascularly active voxels across the entire cord. After delay correction, significantly responding voxels are more diffusely spread over both ventral and dorsal regions, as compared to the original SCVR amplitude map. This agrees with work in the brain showing increased cerebrovascular reactivity estimates after delay correction (19). This effect is more pronounced in the highly-sampled individuals than for the group-level results; this is likely due to inter-individual variation in hemodynamic delay, which makes it sub-optimal to apply the same delay correction to an entire group. However, the limited data available for each subject in the cross-sectional analysis are not sufficient to robustly estimate and correct for their unique voxelwise hemodynamic delay patterns using our current methods.

**Limitations and future directions.** We demonstrate that our fMRI acquisition and modeling approach can produce consistent and meaningful insight into hemodynamics of the human spinal cord. However, there are numerous challenges in robustly mapping SCVR amplitude and delay that should be considered and addressed in future research.

A breathing task, such as breath-holding, is relatively simple to implement and should cause large, detectable variations in the fMRI signal, but is also likely to cause respiration-induced B0 artifacts, time-locked to the task. Fourier-based respiratory RETROICOR (27) nuisance regressors were included to aid fMRI denoising. There may be concern that some of the signal of interest would be fitted by respiratory RETROICOR regressors, instead of the task. Ultimately, these regressors were included because physiological noise modeling techniques with RETROICOR have been shown to be beneficial with noisy spinal cord fMRI data (28). Additionally, these regressors were included in the first-level model, rather than as a separate denoising regression step. The inclusion of RETROICOR denoising in our study may therefore cause SCVR amplitude to be slightly underestimated, and the impact on delay estimation is not yet clear.

In future work, hypercapnia could be achieved using gas inhalation challenges, which may result in a more controlled hypercapnic stimulus that is not time-locked to ventilation, chest position changes, and subsequent B0 effects. Gas inhalation challenges could also increase task compliance, because participants do not need to actively comply with the voluntary breathing task. Indeed, the early spinal cord fMRI work involving a hypercapnic stimulus used different gas inhalation techniques (17, 18). However, the requisite facemask may be less comfortable for participants and less compatible with some coils (e.g., the 64-channel head/neck coil used in this study). Although literature from cerebrovascular reactivity mapping in the brain suggests that these two methods generate similar results (29), future work should be done to compare breath-holding task-based SCVR measurements with those derived from gas inhalation challenges.

The ground truth of our SCVR measurements across spinal cord vascular territories is unknown; it will be important in future work to refine the range and step size of the shifted $P_{ET}CO_2$ regressors. The ±10s $P_{ET}CO_2$ range was informed by previous brain literature using a range of ±9s (30, 31). It is pertinent to note that histograms of gray matter delay showed a high density at the upper boundary of the range (+10s) as well as the presence of voxels with -10s delays directly adjacent to voxels with +10s delays. These voxels may not reflect physiologically plausible SCVR delays. Additionally, in brain literature, with finer (~0.3s) increments, shifts at the upper and lower boundary of the range are not included because they are not considered optimized (19, 30). Considering the coarse 2s shift increment used in this study, boundary delays were not removed. Refinement of the range and step size will be an important target for future work, and evidence from brain literature suggests this may be particularly important in individuals with pathologically delayed blood supply to the cord (30). Additionally, Bayesian modeling of SCVR amplitude and delay, using our initial work to inform spatial priors, could also improve our ability to robustly map individual subject hemodynamics (32).

White matter SCVR measurements were not excluded from amplitude and delay maps. However, relative to gray matter tissue, white matter is less vascularized and has lower SNR; thus, SCVR was not explicitly interpreted in this region. Higher magnetic field strengths are an appealing choice for imaging white matter cerebrovascular reactivity as seen in the brain (33), and future ultra-high field MRI work may similarly boost sensitivity and enable characterization of white matter SCVR.

## 4. Conclusion

SCVR amplitude and delay mapping has the potential to provide clinically relevant information about spinal cord vascular health. Robust maps of SCVR amplitude and delay were presented at the group-level and in two highly-sampled individuals. Hemodynamic delay maps represent the temporal

difference in the BOLD response across the cord and resemble expected territories of arterial supply. Future work to refine these promising noninvasive methods will facilitate our long-term goal to establish SCVR as a clinically relevant metric of spinal cord vascular health.

## 5. Materials and Methods

**Participants.** This study was approved by the Northwestern University Institutional Review Board, and informed consent was obtained for all participants. Two datasets were collected for this study and will be referred to as Group SCVR and Individual SCVR. **Group SCVR dataset**: MRI data were collected from 30 healthy participants (25.9±4.5 years, 19M). Data were excluded for 3 participants due to excessive image artifacts (N=2) and an incidental finding (N=1). All subsequent Group SCVR analyses represent data from the remaining 27 participants (26±5y, 18F). **Individual SCVR dataset**: MRI data were collected from 3 healthy participants (24±3y, 2F). Data were excluded for one participant due to radiofrequency image artifacts. Subsequent Individual SCVR analyses represent data from the remaining 2 participants (26±2y, 2F).

**Data Collection.** Spinal MRI data were acquired on a 3T Siemens Prisma MRI system (Siemens Healthcare, Erlangen, Germany) with a 64-channel head/neck coil. A SatPad™ cervical collar (SatPad Clinical Imaging Solutions, West Chester, PA, USA) was positioned around the posterior of the neck of the participants to increase the homogeneity of the magnetic field around the imaging region. Group SCVR: MRI was acquired before and after the administration of a 30-minute acute intermittent hypoxia (AIH) protocol, as part of a larger research study (see *AIH* in SI Appendix for more details). (Note, AIH had a negligible/non-significant impact.) Individual SCVR: Anatomical and functional scans were acquired in 3 sessions.

**Imaging Protocol.** A high resolution anatomical T2-weighted scan was acquired first. BOLD fMRI scans were acquired in the cervical spinal cord from approximately the C4-C7 vertebral level (see *Imaging Protocol* in SI Appendix for more details). Group SCVR: A spinal cord anatomical and breath-holding task functional scan were acquired during each of the 2 MRI sessions. Additional spinal cord and brain scans were also acquired during the sessions and were not analyzed in this study. Individual SCVR: A spinal cord anatomical and 5-7 breath-holding task functional scans were acquired during each of the 3 MRI sessions. The total number of task runs was 18 for each participant.

**Breath-holding Task Paradigm.** A hypercapnic breath-holding task was used to modulate participants $CO_2$. The fMRI acquisition was about 6.8 minutes (205 volumes). The task began with a 20 second rest, followed by 7 breath-hold cycles, and ended with a 30 second rest period. Each breath-

hold cycle was as follows: 24 seconds paced breathing (3 seconds in, 3 seconds out), 18 second end-expiration breath-hold, 2 second exhalation, 6 second recovery. Exhaled gases ($CO_2$ and $O_2$), respiration, and pulse were collected throughout the task fMRI scans (see *Physiological Monitoring* in SI Appendix for more details).

**fMRI Preprocessing Pipeline.** Images were converted from DICOM to NIFTI format (dcm2niix_afni (34)). 2D slicewise motion correction was applied with the Neptune Toolbox (35) and AFNI (36, 37). Co-registration between native, anatomical, and PAM50 template space (38) was performed with the Spinal Cord Toolbox (39). These warping fields were calculated, but not applied until after subject-level modeling. See *Motion Correction* and *Registration* sections in SI Appendix for more details. Smoothing: Functional data were smoothed using a "restricted smoothing" technique (40), within a mask of the spinal cord. A 2x2x6mm$^3$ full-width half-maximum (FWHM) Gaussian smoothing kernel was used (*3dBlurInMask*). Trimming fMRI Volumes: The first and last 5 volumes were trimmed from the functional data to allow for shifts of the task regressor for hemodynamic delay mapping (discussed later). Percent signal change: The percent signal change was calculated voxelwise: (X-mean(X))/mean(X), where X is the voxel timeseries.

**Task and Nuisance Regressors.** Physiological data ($CO_2$, pulse, and respiratory belt) were preprocessed in a bespoke MATLAB (MathWorks, Natick, MA, R2019b) script. The results of a peak-finding algorithm were manually verified. Breath-holding Task: From the preprocessed $CO_2$ data, an end-tidal $CO_2$ ($P_{ET}CO_2$) task regressor was calculated and convolved with the canonical hemodynamic response function (HRF). Respiratory and Cardiac: From the preprocessed respiration belt and pulse transducer data 8 respiratory and 8 cardiac slicewise RETROICOR (27, 28) regressors were calculated. Only cardiac regressors were calculated for one subject without belt data. Cerebrospinal fluid (CSF): An initial CSF mask was defined; high variance (top 20% in each slice) voxels were retained in the mask and the average timeseries within this mask was used to create slicewise CSF regressor (28, 41).

**fMRI Analysis.** First-level Analysis: FSL (42) (version 6.0.3) was used to calculate the first-level fMRI models (FEAT (43)). The first-level models contained the $P_{ET}CO_2$ task regressor and 19 nuisance regressors (2 motion, 16 RETROICOR, 1 CSF). FILM (FMRIB's Improved Linear Model) prewhitening was used; the high-pass filter cutoff was set to 100 seconds and all input regressors were demeaned. One statistical contrast was defined: $P_{ET}CO_2>0$. Output files were warped from subject functional space to the PAM50 template space. Higher-level Analysis: The "contrast of parameter estimate" (COPE) maps were averaged across the two sessions within each subject (Group SCVR). A group spinal cord mask was calculated as the consensus region of the co-registered first-level results, and higher-level analyses were performed within this mask, only. This mask was calculated separately for the Group SCVR and Individual SCVR studies. A non-parametric one-sample t-test using threshold-

free cluster enhancement (TFCE) and 5000 permutations was used to calculate the higher-level activation maps with family-wise error (FWE) rate correction (*randomise*) (44–46). The average parameter estimates are the SCVR amplitude.

**Reliability of Individual SCVR Estimates.** To probe the reliability of SCVR estimates for different amounts of data, a split-halves analysis was used (20). For each subject, the 18 COPE maps were randomly split into 2 halves, comparing subsets of one half (1-9 runs) to the other 9 runs combined via spatial Pearson correlation in the ventral gray matter. This was repeated 1000 times to build a distribution. Average SCVR in the ventral gray matter was also considered by incrementally combining runs from 1 run to all 18 runs. This was done in the originally acquired order of fMRI runs and then for 100 randomly shuffled orders.

**SCVR Hemodynamic Delay.** 10 temporally shifted versions of the $P_{ET}CO_2$ regressor were created to allow for timing differences of ±10s in the increment of the TR (2s). First-level models were repeated identically to the original except for the temporally shifted $P_{ET}CO_2$ regressor. The higher-level analyses in PAM50 space were also repeated for each shift. For each voxel, the highest t-statistic across the delay range was designated as the optimal shift (the "delay" for that voxel) (*getBestFits()*). <u>Delay-corrected SCVR Amplitude</u>: These optimal shifts were then used to create a delay-corrected SCVR map. For each run, delay-corrected COPE maps were generated using the parameter estimates associated with the optimal shift (*delayCorrectedSCVR()*). This resulted in delay-corrected COPE maps for each run, which were then processed with the same higher-level analyses used previously. The average parameter estimates are the delay-corrected SCVR amplitude. <u>Delay-based Segmentation</u>: A histogram of gray matter delays was manually thresholded. Voxels with delays on either side of the threshold were designated as *Region 1* (Earlier) or *Region 2* (Later).

## References


1. N. L. Martirosyan, *et al.*, Blood supply and vascular reactivity of the spinal cord under normal and pathological conditions: A review. *J Neurosurg Spine* **15** (2011).
2. A. Nouri, L. Tetreault, A. Singh, S. K. Karadimas, M. G. Fehlings, Degenerative cervical myelopathy: Epidemiology, genetics, and pathogenesis. *Spine (Phila Pa 1976)* **40** (2015).
3. F. Eippert, Y. Kong, M. Jenkinson, I. Tracey, J. C. W. Brooks, Denoising spinal cord fMRI data: Approaches to acquisition and analysis. *Neuroimage* **154**, 255–266 (2017).
4. N. Kinany, E. Pirondini, S. Micera, D. Van De Ville, Spinal Cord fMRI: A New Window into the Central Nervous System. *Neuroscientist* **29**, 715–731 (2022).
5. B. M. Ellingson, D. C. Woodworth, K. Leu, N. Salamon, L. T. Holly, Spinal Cord Perfusion MR Imaging Implicates Both Ischemia and Hypoxia in the Pathogenesis of Cervical Spondylosis. *World Neurosurg* **128** (2019).
6. K. Uemura, *et al.*, Perfusion-weighted magnetic resonance imaging of the spinal cord in cervical spondylotic myelopathy. *Neurol Med Chir (Tokyo)* **46** (2006).
7. T. Kanda, *et al.*, Gadolinium-based contrast agent accumulates in the brain even in subjects without severe renal dysfunction: Evaluation of autopsy brain specimens with inductively coupled plasma mass spectroscopy. *Radiology* **276**, 228–232 (2015).
8. G. H. Jahng, K. L. Li, L. Ostergaard, F. Calamante, Perfusion magnetic resonance imaging: A comprehensive update on principles and techniques. *Korean J Radiol* **15**, 554–577 (2014).
9. G. Frébourg, *et al.*, “Dynamic Contrast Enhanced MR perfusion of the Spinal Cord with radial streaking artefacts reduction at 3T: Preliminary results and applications” in *Proceedings 30th Scientific Meeting, International Society for Magnetic Resonance in Medicine*, (2022).
10. B. P. Meyer, *et al.*, Optimized cervical spinal cord perfusion MRI after traumatic injury in the rat. *Journal of Cerebral Blood Flow and Metabolism* **41** (2021).
11. S. Lee, N. Wilkins, B. D. Schmit, S. N. Kurpad, M. D. Budde, Relationships between spinal cord blood flow measured with flow-sensitive alternating inversion recovery (FAIR) and neurobehavioral outcomes in rat spinal cord injury. *Magn Reson Imaging* **78**, 42–51 (2021).
12. G. Nair, X. P. Hu, “Perfusion Imaging of the Human Cervical Spinal Cord” in *Proceedings 18th Scientific Meeting, International Society for Magnetic Resonance in Medicine*, (2010).
13. O. M. Girard, V. Callot, B. Robert, P. J. Cozzone, G. Duhamel, “Perfusion MRI of the Human Cervical Spinal Cord using Arterial Spin Labeling” in *Proceedings 21st Scientific Meeting, International Society for Magnetic Resonance in Medicine*, (2013).
14. S. Lévy, *et al.*, Intravoxel Incoherent Motion at 7 Tesla to quantify human spinal cord perfusion: limitations and promises. *Magn Reson Med* **84**, 1198–1217 (2020).

15. J. Pinto, M. G. Bright, D. P. Bulte, P. Figueiredo, Cerebrovascular Reactivity Mapping Without Gas Challenges: A Methodological Guide. *Front Physiol* **11** (2021).
16. A. L. Urback, B. J. MacIntosh, B. I. Goldstein, Cerebrovascular reactivity measured by functional magnetic resonance imaging during breath-hold challenge: A systematic review. *Neurosci Biobehav Rev* **79**, 27–47 (2017).
17. J. Cohen-Adad, *et al.*, BOLD signal responses to controlled hypercapnia in human spinal cord. *Neuroimage* **50**, 1074–1084 (2010).
18. R. L. Barry, *et al.*, Multi-shot acquisitions for stimulus-evoked spinal cord BOLD fMRI. *Magn Reson Med* **85**, 2016–2026 (2021).
19. S. Moia, *et al.*, Voxelwise optimization of hemodynamic lags to improve regional CVR estimates in breath-hold fMRI. *Annu Int Conf IEEE Eng Med Biol Soc* **2020**, 1489–1492 (2020).
20. T. O. Laumann, *et al.*, Functional System and Areal Organization of a Highly Sampled Individual Human Brain. *Neuron* **87**, 657–670 (2015).
21. K. C. Kang, T. S. Jang, S. H. Choi, H. W. Kim, Difference between Anterior and Posterior Cord Compression and Its Clinical Implication in Patients with Degenerative Cervical Myelopathy †. *J Clin Med* **12** (2023).
22. K. J. Hemmerling, M. A. Hoggarth, M. S. Sandhu, T. B. Parrish, M. G. Bright, Spatial distribution of hand-grasp motor task activity in spinal cord functional magnetic resonance imaging. *Hum Brain Mapp* **44**, 5567–5581 (2023).
23. M. G. Bright, K. Murphy, Reliable quantification of BOLD fMRI cerebrovascular reactivity despite poor breath-hold performance. *Neuroimage* **83**, 559–568 (2013).
24. J. Pinto, J. Jorge, I. Sousa, P. Vilela, P. Figueiredo, Fourier modeling of the BOLD response to a breath-hold task: Optimization and reproducibility. *Neuroimage* **135**, 223–231 (2016).
25. A. E. Mautes, M. R. Weinzierl, F. Donovan, L. J. Noble, Vascular Events After Spinal Cord Injury: Contribution to Secondary Pathogenesis Spinal Cord Injury Special Series. *Phys Ther* **80**, 673–687 (2000).
26. C. H. Tator, I. Koyanagi, Vascular mechanisms in the pathophysiology of human spinal cord injury. *J Neurosurg* **86**, 483–492 (1997).
27. G. H. Glover, T. Q. Li, D. Ress, Image-based method for retrospective correction of physiological motion effects in fMRI: RETROICOR. *Magn Reson Med* **44**, 162–167 (2000).
28. J. C. W. Brooks, *et al.*, Physiological noise modelling for spinal functional magnetic resonance imaging studies. *Neuroimage* **39**, 680–692 (2008).
29. A. Kastrup, G. Krüger, T. Neumann-Haefelin, M. E. Moseley, Assessment of cerebrovascular reactivity with functional magnetic resonance imaging: Comparison of CO2 and breath holding. *Magn Reson Imaging* **19**, 13–20 (2001).

30. R. C. Stickland, *et al.*, A practical modification to a resting state fMRI protocol for improved characterization of cerebrovascular function. *Neuroimage* **239** (2021).
31. K. M. Zvolanek, *et al.*, Comparing end-tidal CO2, respiration volume per time (RVT), and average gray matter signal for mapping cerebrovascular reactivity amplitude and delay with breath-hold task BOLD fMRI. *Neuroimage* **272** (2023).
32. J. Pinto, *et al.*, "Evaluating cerebrovascular reactivity dynamics through a Bayesian inference approach" in *Proceedings 30th Scientific Meeting, International Society for Magnetic Resonance in Medicine*, (2022).
33. A. A. Bhogal, *et al.*, Examining the regional and cerebral depth-dependent BOLD cerebrovascular reactivity response at 7T. *Neuroimage* **114**, 239–248 (2015).
34. X. Li, P. S. Morgan, J. Ashburner, J. Smith, C. Rorden, The first step for neuroimaging data analysis: DICOM to NIfTI conversion. *J Neurosci Methods* **264**, 47–56 (2016).
35. R. Deshpande, R. Barry, "Neptune: a toolbox for spinal cord functional MRI data processing and quality assurance" in *Proceedings 30th Scientific Meeting, International Society for Magnetic Resonance in Medicine*, (2022).
36. R. W. Cox, AFNI: Software for analysis and visualization of functional magnetic resonance neuroimages. *Computers and Biomedical Research* **29**, 162–173 (1996).
37. R. W. Cox, J. S. Hyde, Software tools for analysis and visualization of fMRI data. *NMR Biomed* **10**, 171–178 (1997).
38. B. De Leener, *et al.*, PAM50: Unbiased multimodal template of the brainstem and spinal cord aligned with the ICBM152 space. *Neuroimage* **165**, 170–179 (2018).
39. B. De Leener, *et al.*, SCT: Spinal Cord Toolbox, an open-source software for processing spinal cord MRI data. *Neuroimage* **145**, 24–43 (2017).
40. K. Hemmerling, M. Bright, "Restricted smoothing of spinal cord fMRI data resolves structured temporal variation in heatmaps" in *Proceedings 27th Scientific Meeting, Organization for Human Brain Mapping*, (2021).
41. Y. Kong, M. Jenkinson, J. Andersson, I. Tracey, J. C. W. Brooks, Assessment of physiological noise modelling methods for functional imaging of the spinal cord. *Neuroimage* **60**, 1538–1549 (2012).
42. M. Jenkinson, C. F. Beckmann, T. E. J. Behrens, M. W. Woolrich, S. M. Smith, FSL. *Neuroimage* **62**, 782–790 (2012).
43. M. W. Woolrich, B. D. Ripley, M. Brady, S. M. Smith, Temporal Autocorrelation in Univariate Linear Modeling of FMRI Data. *Neuroimage* **14**, 1370–1386 (2001).
44. A. M. Winkler, G. R. Ridgway, M. A. Webster, S. M. Smith, T. E. Nichols, Permutation inference for the general linear model. *Neuroimage* **92**, 381–397 (2014).

45. S. M. Smith, T. E. Nichols, Threshold-free cluster enhancement: Addressing problems of smoothing, threshold dependence and localisation in cluster inference. *Neuroimage* **44**, 83–98 (2009).
46. T. E. Nichols, A. P. Holmes, Nonparametric Permutation Tests For Functional Neuroimaging: A Primer with Examples. *Hum Brain Mapp* **15**, 1–25 (2002).